

Structural Characterization of Molybdenum Oxide Nanoclusters Using Ion Mobility Spectrometry–Mass Spectrometry and Infrared Action Spectroscopy

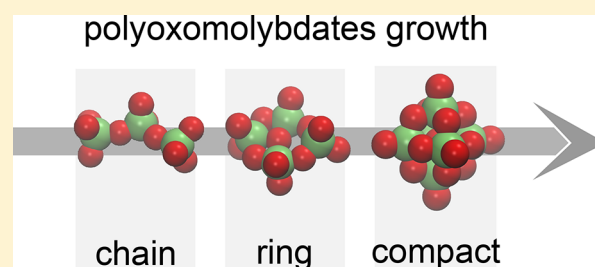
Mateusz Marianski,^{†,¶} Jongcheol Seo,^{†,¶} Eike Mucha,[†] Daniel A. Thomas,[†] Sabrina Jung,[†] Robert Schlögl,^{†,‡} Gerard Meijer,[†] Annette Trunschke,^{*,†,‡} and Gert von Helden^{*,†,‡}

[†]Fritz-Haber-Institut der Max-Planck-Gesellschaft, Faradayweg 4-6, 14195 Berlin, Germany

[‡]Max-Planck-Institut für Chemische Energiekonversion, Stiftstrasse 34-36, 45470 Mülheim an der Ruhr, Germany

Supporting Information

ABSTRACT: Polyoxometalate clusters possess unique catalytic and electromagnetic properties. The structure and function of polyoxometalates is dictated by complex oligomerization processes, which in turn depend on the solution conditions. In this work, small gas-phase polyoxomolybdate nanoclusters ($\text{HMo}_n\text{O}_{3n+1}^-$, $n = 1-8$, and $\text{Mo}_n\text{O}_{3n+1}^{2-}$, $n = 2-8$) were investigated after nano-electrospray of an acidified solution of ammonium heptamolybdate heptahydrate by ion mobility spectrometry–mass spectrometry (IMS–MS), infrared multiple photon dissociation (IRMPD) spectroscopy, and infrared action spectroscopy in helium nanodroplets. The spectra and collision cross sections obtained were matched to predictions from density-functional theory (DFT) to unravel the structural progression of nanoclusters with increasing size. For doubly charged clusters, transitions among chain ($n = 2-3$), ring ($n = 4-5$), and compact ($n \geq 6$) structures are observed in IMS–MS and IR spectroscopy experiments, in agreement with low-energy structures from DFT calculations. For singly charged clusters, reduced Coulombic repulsion and hydrogen bonding interactions are found to strongly influence the most stable cluster structure. Notably, a noncovalent ring structure is observed for $\text{HMo}_3\text{O}_{10}^{1-}$, stabilized by a strong intramolecular hydrogen bond, and a compact structure is observed for $\text{HMo}_5\text{O}_{16}^{1-}$, in contrast to the ring structure favored for $\text{Mo}_5\text{O}_{16}^{2-}$.



INTRODUCTION

Polyoxometalate (POM) clusters of early transition metals such as vanadium, molybdenum, and tungsten are of great interest, because their wide range of electromagnetic, optical, and catalytic properties have opened new research avenues in numerous fields, including materials science,¹ inorganic catalysis,²⁻⁴ molecular electronic devices,⁵ and therapeutics.⁶ POMs form by condensation reactions in solution, and variation of the reaction conditions can result in clusters ranging in size from nano to micrometers that exhibit a variety of structural motifs. In the solid state, there are several well-known, stable motifs, such as Keggin,⁷ Anderson,^{8,9} Dawson,^{10,11} and Lindqvist^{12,13} structures, which feature well-defined POM clusters ideal for the aforementioned applications.

The functional properties of nanostructured POM-derived materials are strongly affected by the oligomerization pathways in solution, which are initiated by the dynamic self-assembly reactions of oxyanions in acidic media. However, their growth and assembly mechanisms, especially in the early stages of condensation, are largely unclear, as the polydisperse nature of POM clusters impedes facile characterization of the nucleation process. Specifically, standard condensed-phase techniques probe only the ensemble-average state of the wide range of

cluster sizes, shapes, and charge states present, and the structures of individual clusters typically cannot be resolved.

This limitation can be overcome by employing complementary gas-phase techniques that utilize ion mobility spectrometry (IMS) and mass spectrometry (MS). The combination of these methods provides selection of clusters of well-defined sizes: IMS and MS are able to separate and isolate ions by their geometrical collision cross-section (CCS)-to-charge ratio (CCS/ z) and mass-to-charge ratio (m/z), respectively. When utilized with electrospray ionization (ESI), which can transfer intact cluster ions from solution to the gas phase, IMS–MS can yield insight into the overall size and shape of each observed cluster ion.^{14,15}

Although IMS–MS provides useful information on the overall geometry of a cluster ion, the method is largely insensitive to the internal structure. However, IR action spectroscopy can be used to obtain details of the binding and geometric arrangement of atoms within a cluster. Coupling IR

Special Issue: Hans-Joachim Freund and Joachim Sauer Festschrift

Received: July 20, 2018

Revised: August 31, 2018

Published: September 7, 2018

action spectroscopy to either MS alone or to IMS–MS provides vibrational spectra of clusters that are either m/z - or both m/z - and CCS/ z -selected. Notably, infrared multiple photon dissociation (IRMPD) spectroscopy¹⁶ combined with IMS–MS has been shown to provide high sensitivity and selectivity and has been utilized recently to investigate a range of biomolecular clusters.^{17,18} In addition, IR action spectroscopy of m/z -selected molecular ions captured and cooled to ~ 0.4 K in helium nanodroplets has been demonstrated to yield well-resolved IR bands for complex species.^{19,20} The exceptionally high resolution of IR spectra of small ions encapsulated in helium nanodroplets provides a deeper insight into the internal structure of ions than available from IRMPD.^{21,22} The combination of CCS values and IR spectra provides a detailed picture of cluster structure that can be matched to predictions from electronic-structure theory calculations to elucidate structural details at the atomic level.^{23–25}

Previous studies have demonstrated the utility of mass-spectrometry-based techniques for the analysis of POMs. ESI-MS-based approaches have been used to investigate architectures of different POM clusters as well as to understand the nucleation process of metal oxides^{26–41} and zeolites.^{42–44} The formation of Lindqvist $W_6O_{19}^{2-}$ and $Mo_6O_{19}^{2-}$ anions was tracked by ESI-MS by Vilá-Nadal et al.,^{32,33} and the self-assembly kinetics of hybrid POMs has been studied in real time.^{31,34,35,37,38} More recently, IMS–MS has been applied to obtain further insight into the geometric structure of POM clusters.^{15,45–48} Similarly, IRMPD spectroscopy has been applied to unravel the structures of several metal and metal oxide cluster ions, including gold nanoclusters,^{49,50} iron oxide⁵¹ and vanadium oxide clusters,⁵² and tantalum and niobium oxide clusters.⁵³ These experimental studies are frequently accompanied by density-functional theory (DFT) calculations, which have a long history of successes in the investigation of the properties of metal oxides in bulk^{54,55} and cluster models.^{56–58}

In the present work, we combine ESI-IMS–MS, IRMPD, IR spectroscopy in helium nanodroplets, and DFT to investigate the structures and the assembly process of early polyoxomolybdate cluster anions ($HMo_nO_{3n+1}^{1-}$, $n = 1–8$, and $Mo_nO_{3n+1}^{2-}$, $n = 2–8$). The combination of these techniques allows us to assess in detail the size and shape of each cluster as well as to evaluate the internal Mo–O bonding structure.

MATERIALS AND METHOD

All chemicals were obtained from Merck KGaA (Darmstadt, Germany). Aqueous solutions of ammonium heptamolybdate heptahydrate (35 mM) were prepared and adjusted to pH values of 9 or 3 by the addition of ammonium hydroxide or nitric acid.

The experimental setup utilized for IMS–MS and IRMPD experiments has been described previously,^{59,60} and only a brief outline is given here. Gas-phase ions were generated from solution via a nanoESI source and transferred through a capillary inlet into the trapping region of the apparatus. Ions were then pulsed into a helium-filled (4–5 mbar) drift cell, where they were separated according to their CCS/ z by the application of a weak electric field (10–15 V cm^{-1}). After this ion mobility separation, a quadrupole mass filter was utilized for m/z selection. The time-dependent ion current of an m/z -selected cluster ion was measured to obtain the arrival time distribution (ATD), which was subsequently utilized to determine the CCS. For IRMPD spectroscopy, ions were

first selected according to their CCS/ z and m/z and then irradiated by IR photons generated by the Fritz-Haber-Institut free-electron laser (FHI FEL).⁶¹ The absorption of a sufficient number of resonant photons resulted in ion dissociation, which was monitored by time-of-flight (TOF) mass spectrometry. The IRMPD spectrum was obtained by plotting the IR-induced fragmentation yield as a function of IR wavelength.

The apparatus utilized to collect infrared action spectra of cluster ions captured in He nanodroplets has also been described in prior publications.^{20,62} In short, gas-phase cluster ions were produced by nanoESI, transferred to vacuum, and m/z -selected utilizing a quadrupole mass filter. The selected cluster ions were then transferred to an orthogonal hexapole ion trap by means of a DC ion bender and stored for several seconds. A pulsed beam of helium nanodroplets was directed through the ion trap, resulting in cluster-ion capture by the nanodroplets. Following evaporative cooling to an equilibrium temperature of ~ 0.4 K, the nanodroplets with an entrained cluster ion contained on average 50 000 He atoms.⁶³ Due to their large kinetic energy, the charged nanodroplets were able to escape the shallow potential well of the ion trap and enter a TOF MS extraction region, where they were irradiated with infrared photons produced by the FHI FEL.⁶¹ The absorption of multiple resonant photons resulted in the production of bare ions that were monitored by TOF MS, and the infrared spectrum was obtained as the integrated intensity in a given m/z range as a function of the incident photon energy.

Candidate molybdenum oxide structures were optimized using DFT theory by applying the PBE exchange-correlation functional⁶⁴ augmented with vdW^{TS} correction for long-range dispersion⁶⁵ with tight basis set settings using the FHI-aims all electron code.⁶⁶ For the lowest-energy structures found for each cluster, CCS values were calculated using the projection approximation,⁶⁷ and IR spectra were computed in the harmonic approximation. The details of the calculations as well as xyz-coordinates of optimized structures are given in the Supporting Information.

RESULTS AND DISCUSSION

Figure 1 shows typical nanoESI-TOF mass spectra obtained from molybdenum oxide solutions at pH 9 and 3. Under basic solution conditions (pH 9), signal from the singly charged monomolybdate ion ($HMoO_4^-$) dominates the mass spectrum (Figure 1, top). However, when the pH of the solution is decreased to 3, the $HMoO_4^-$ peak is significantly reduced in intensity, and a series of peaks corresponding to doubly charged polyoxomolybdate ions appears ($Mo_nO_{3n+1}^{2-}$, $n = 2–11$; Figure 1, bottom). Singly charged polyoxomolybdate cluster ions ($HMo_nO_{3n+1}^{1-}$, $n = 1–8$) are also detected at a lower relative intensity. Due to the broad isotopic distribution of molybdenum, overlap between the isotopic envelope of the singly charged and doubly charged polyoxomolybdate ions is observed in the mass spectrum for larger cluster sizes. The polyoxomolybdate ions generated from nanoESI of the pH 3 solution were analyzed utilizing IMS–MS to obtain ATDs and derive CCS values as well as to perform IR action spectroscopy experiments. The m/z -selected ATDs for most cluster ions were found to exhibit only a single peak (Figure S1), indicating the presence of a single geometrical isomer. The $HMo_4O_{13}^{1-}$ cluster ion was found to exhibit a broadened feature in the ATD, potentially indicating the presence of multiple structures with only small differences in CCS.

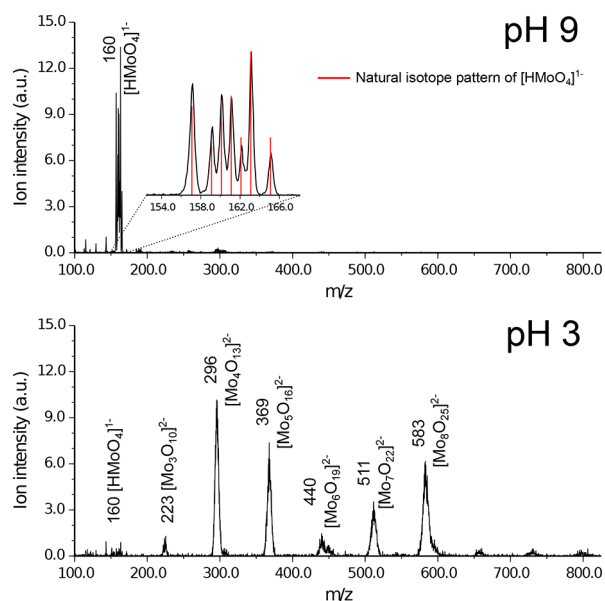


Figure 1. Mass spectra of molybdenum oxide ions at pH 9 (top) and pH 3 (bottom) collected by nanoESI-TOF-MS. Whereas at basic pH, solely the HMoO_4^- ion is present in the mass spectrum, an acidic pH promotes the formation of condensates, notably $\text{Mo}_n\text{O}_{3n+1}^{2-}$ ($n = 2-11$) and $\text{HMo}_n\text{O}_{3n+1}^{1-}$ ($n = 1-8$) ions.

Doubly Charged Polyoxomolybdate Clusters. Figure 2 summarizes the results obtained from IMS-MS analysis of the

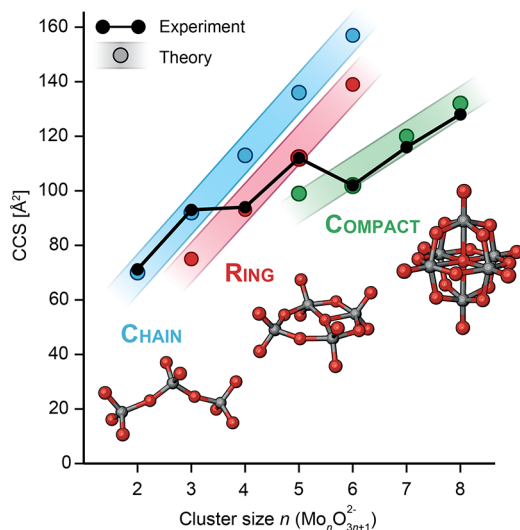


Figure 2. Experimental vs theoretical CCS values for doubly charged polyoxomolybdate clusters $\text{Mo}_n\text{O}_{3n+1}^{2-}$ ($n = 2-8$). CCS values are plotted as a function of the number of molybdenum atoms in the cluster n , with experimental values shown in black, and predicted CCS values for model structures with a chain, ring, and compact motif shown in blue, red, and green, respectively.

doubly charged polyoxomolybdate cluster anions. The CCS values obtained for $\text{Mo}_n\text{O}_{3n+1}^{2-}$ ($n = 2-8$) are plotted as a function of the number of Mo atoms (black circles), with the lines connecting points serving as a guide for the eye. Notably, the CCS does not increase smoothly with the number of Mo atoms but rather exhibits prominent discontinuities between $n = 3$ and $n = 4$ and between $n = 5$ and $n = 6$.

To assess the changes in structure leading to the observed discontinuities in the CCS values of the doubly charged polyoxomolybdate clusters with size, the experimental CCS of each cluster was compared to the theoretical CCS values calculated for low-energy, DFT-optimized structures. The predicted CCS values for these structures are shown in Figure 2 as colored circles, and numerical values are listed in Table S1 of the Supporting Information. Three structural classes were considered: chain structures (blue circles), in which MoO_4 tetrahedra are connected via a bridging oxygen atom; ring structures (red circles), in which each molybdenum oxide unit is coordinated to two neighboring units; and compact structures (green circles), in which molybdenum oxide units exhibit a complex and often highly symmetric three-dimensional coordination. The experimental cross sections for $\text{Mo}_2\text{O}_7^{2-}$ and $\text{Mo}_3\text{O}_{10}^{2-}$ exhibit excellent agreement with theoretical CCS values for the corresponding chain structure. For $\text{Mo}_3\text{O}_{10}^{2-}$, a chain structure is calculated to be $21.7 \text{ kcal mol}^{-1}$ more stable than a ring structure. However, when an additional molybdenum oxide unit is added, forming $\text{Mo}_4\text{O}_{13}^{2-}$, the bond angles for ring formation become more favorable, and a ring structure is calculated to be more stable than its linear counterpart by $6.0 \text{ kcal mol}^{-1}$. The experimental CCS for $\text{Mo}_4\text{O}_{13}^{2-}$ also closely matches the predicted CCS for the theoretical ring structure. For $\text{Mo}_5\text{O}_{16}^{2-}$, three different low-energy ring conformers were found (Figure S2), differing in energy by less than $0.2 \text{ kcal mol}^{-1}$ following vibrational zero-point correction and all exhibiting CCS values matching well to experiment. In addition, all of these structures were appreciably lower in energy than chain or compact structures. The notable reduction in cross section between $\text{Mo}_5\text{O}_{16}^{2-}$ and $\text{Mo}_6\text{O}_{19}^{2-}$ corresponds well to the predicted change in CCS upon transition from a ring structure to a compact structure. The highly symmetric and compact three-dimensional Lindqvist structure for $\text{Mo}_6\text{O}_{19}^{2-}$ is also significantly more stable than either a ring or chain motif.

For $\text{Mo}_7\text{O}_{22}^{2-}$ and $\text{Mo}_8\text{O}_{25}^{2-}$, several subfamilies of compact, three-dimensional structures were identified from DFT calculations, as shown in Figure S3. The experimental CCS for $\text{Mo}_7\text{O}_{22}^{2-}$ matches most closely to a modified Lindqvist structure, in which the seventh molybdenum oxide unit is located external to a Lindqvist core. This structure is also predicted to be more stable than a compact symmetric structure incorporating all seven molybdenum oxide units. An expanded symmetric structure featuring a ring of six molybdenum oxide units was found to be $8.5 \text{ kcal mol}^{-1}$ more stable than the Lindqvist structure, but the predicted CCS value of 129 \AA^2 is in poor agreement with experiment. For $\text{Mo}_8\text{O}_{25}^{2-}$, in contrast, the expanded symmetric structure has a predicted CCS of 128 \AA^2 , in excellent agreement with experiment, and is predicted to be more stable than a Lindqvist-derived structure by $10.0 \text{ kcal mol}^{-1}$. Candidate structures for $\text{Mo}_8\text{O}_{25}^{2-}$ are shown in Figure S4.

To further probe the internal structure of the clusters, room-temperature action spectra in the range of $700-1000 \text{ cm}^{-1}$ were obtained using m/z - and CCS/z -selected IRMPD spectroscopy. Additionally, cold-ion action spectra were acquired on a separate instrument by m/z -selected IR action spectroscopy of cluster ions cooled to $\sim 0.4 \text{ K}$ following capture in helium nanodroplets. Shown in Figure 3 are the spectra for $\text{Mo}_n\text{O}_{3n+1}^{2-}$ ($n = 2-7$) obtained using IRMPD spectroscopy (red) and action spectroscopy in helium nanodroplets (blue). The IRMPD spectrum of $\text{Mo}_8\text{O}_{25}^{2-}$ is

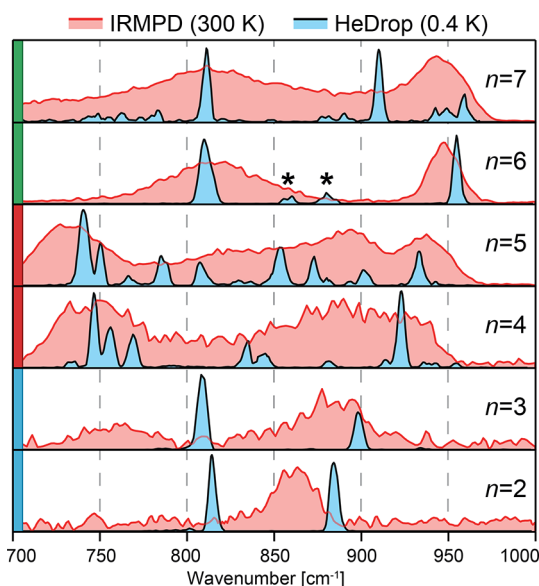


Figure 3. Action infrared spectra of $\text{Mo}_n\text{O}_{3n+1}^{2-}$ ($n = 2-7$) obtained utilizing IRMPD spectroscopy of room-temperature ions (red) and IR spectroscopy of ions captured in helium nanodroplets (blue). Prominent changes in the spectra are observed between $n = 3$ and $n = 4$ as well as between $n = 5$ and $n = 6$, reflecting significant structural changes during growth of the polyoxomolybdate clusters.

shown in Figure S4 of the Supporting Information. Upon initial inspection, both the IRMPD and the cold-ion IR spectra seem to fall into three groups: (a) spectra of $n = 2$ and 3, which are characterized by two narrow bands in the cold-ion IR spectrum (broad bands in the case of IRMPD), (b) spectra of $n = 4$ and 5, which show a significantly increased number of bands with shifted positions, and (c) spectra of $n = 6$ and 7, which exhibit a small number of intense bands. These groupings correlate well with the changes in CCS values visible in Figure 2.

Clearly, the IRMPD spectra are much broader than the corresponding cold-ion spectra. Although generation of the action signal in He nanodroplet IR spectroscopy requires the absorption of many photons, each absorption event occurs from the vibrational ground state of the cold ion at 0.4 K.^{19,21,22} To generate the action signal in IRMPD spectra, on the other hand, multiple photons are absorbed without dissipation of energy to an external bath, leading to a gradual increase in cluster temperature during the several μs duration interaction time with the infrared radiation and ultimately resulting in dissociation.¹⁶ The result is that anharmonicities as well as cross-anharmonicities can cause significant broadenings, shifts (in general to lower frequencies), and changes in relative intensities. In extreme cases, for very anharmonic modes, vibrational modes can shift out of resonance before sufficient energy to induce dissociation is deposited into the cluster, with the effect that such a mode is not observed in the IRMPD spectrum. This might be the reason why there is no IRMPD counterpart to the band in the cold-ion spectrum near 800 cm^{-1} for $\text{Mo}_2\text{O}_7^{2-}$.

The experimental CCS values for $\text{Mo}_n\text{O}_{3n+1}^{2-}$ clusters support a structural transition from linear to cyclic to three-dimensional motifs. Do the IR spectra support this assignment? Figure 4 compares the IR spectra obtained by the helium nanodroplet method (blue) to unscaled theoretical harmonic spectra convoluted with Gaussian distributions with a full width at

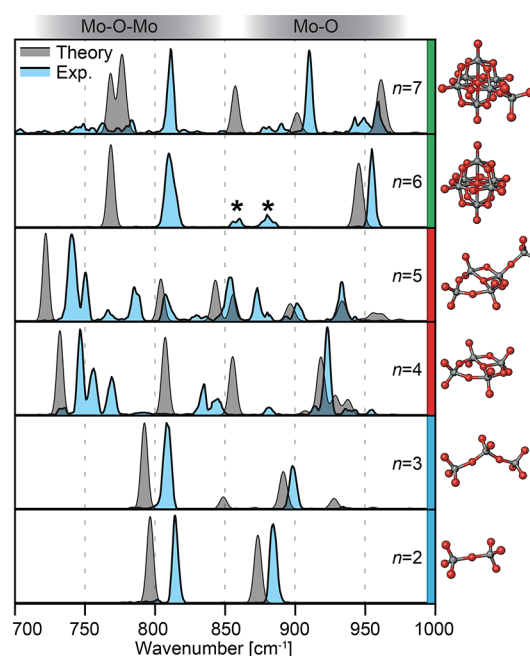


Figure 4. Comparison of experimental IR action spectra of ions captured in helium nanodroplets (blue) and unscaled theoretical IR spectra convoluted with Gaussian distributions with full width at half-maximum values of 0.7% (gray) for $\text{Mo}_n\text{O}_{3n+1}^{2-}$ ($n = 2-7$). The corresponding structure for each theoretical spectrum is shown at the right. For $n = 6$, bands labeled with * originate from $\text{HMo}_3\text{O}_{10}^{1-}$ due to overlapping isotopic distributions.

half-maximum of 0.7% (gray). The corresponding cluster structures are shown to the right. With the exception of the case of $\text{Mo}_7\text{O}_{22}^{2-}$ vide infra, all structures represent the lowest-energy configuration found. In general, the agreement between theory and experiment is reasonable, verifying the transitions from linear to chain to three-dimensional clusters.

In the spectra, theory predicts the fundamental transitions of terminal oxygen stretching (Mo–O) modes to occur between 850 and 1000 cm^{-1} , whereas the fundamental transitions of antisymmetric Mo–O–Mo stretching modes are predicted between 700 and 850 cm^{-1} . In both experiment and theory, a blue-shift of the Mo–O stretching modes is observed with increasing cluster size, reflecting an increase in the strength of the terminal Mo–O bonds. Such a shift is in agreement with the experimentally observed increase in the energy of the Mo–O stretching mode in molybdenum oxide species supported on alumina with increasing molybdenum loading,^{68,69} which has been attributed to oligomerization of MoO_4^{2-} species.⁷⁰ In this respect, the present model studies are complementary to UHV studies of thin film models,⁷¹ and contribute to an improved interpretation of the spectroscopic fingerprints observed in Mo-oxide-based functional materials.^{72,73}

For $\text{Mo}_2\text{O}_7^{2-}$ and $\text{Mo}_3\text{O}_{10}^{2-}$, experiment and theory show good agreement, with an intense feature observed for both the Mo–O and Mo–O–Mo stretching modes. For $\text{Mo}_4\text{O}_{13}^{2-}$ and $\text{Mo}_5\text{O}_{16}^{2-}$, the Mo–O–Mo stretching modes exhibit a red-shift compared to both smaller and larger clusters, possibly as a result of strain and/or weaker bonds to bridging oxygen atoms in the ring conformation.

When comparing the experimental to the theoretical spectra for $\text{Mo}_4\text{O}_{13}^{2-}$ and $\text{Mo}_5\text{O}_{16}^{2-}$, many bands are replicated; however, the overall number of absorption bands is higher in the experimental spectra. This result suggests that there may be

contributions from multiple structures. As discussed in the context of the IMS–MS experiments, theory predicts multiple low-energy structures for at least $\text{Mo}_5\text{O}_{16}^{2-}$, and in the experiment, multiple closely related structures that cannot be separated by IMS–MS might be present, leading to an increased number of bands. For $\text{Mo}_5\text{O}_{16}^{2-}$, a comparison of the experimental IR spectrum to the theoretical spectra for all low-energy structures is shown in Figure S2.

An interesting case is the $\text{Mo}_6\text{O}_{19}^{2-}$ ion. In the experimental cold-ion IR spectrum, only two bands are observed (the bands marked with * originate from $\text{HMo}_3\text{O}_{10}^{1-}$ due to overlapping isotopic envelopes). Such a band pattern is expected for a highly symmetric structure, and indeed, theory predicts the highly symmetric Lindqvist structure to be lowest in energy. Its calculated spectrum features only two bands with frequencies that are in qualitative agreement with the experiment.

For larger clusters, candidate structures that are based on the Lindqvist motif are also plausible. For $\text{Mo}_7\text{O}_{22}^{2-}$, the predicted spectrum for such a modified Lindqvist structure shows qualitative agreement with experiment in the Mo–O stretching region, but the Mo–O–Mo stretching fundamentals are not accurately reproduced. For $\text{Mo}_6\text{O}_{19}^{2-}$, which can be confidently assigned to a Lindqvist structure, such a disagreement is observed as well, suggesting that the DFT method employed systematically underpredicts the energy of this vibrational mode for this structural motif. When considering alternative structures for $\text{Mo}_7\text{O}_{22}^{2-}$, the theoretical spectrum of the more symmetric compact structure (Figure S3d) does not show improved agreement with the experimental spectrum. The alternate expanded structure shows good agreement with the experimental spectrum in the Mo–O–Mo stretching region but not in the Mo–O stretching region (Figure S3e), and the discrepancy between the predicted and experimental CCS value suggests this structure is not observed experimentally. For $\text{Mo}_8\text{O}_{25}^{2-}$, theoretical IR spectra of candidate structures are compared to the IRMPD spectrum in Figure S4, but the unresolved bands in the experimental spectrum prevent a confident structural assignment. IR spectra could not be obtained in He nanodroplets, as the $\text{Mo}_8\text{O}_{25}^{2-}$ and $\text{HMo}_4\text{O}_{13}^{1-}$ could not be isolated with m/z selection alone.

Singly Charged Polyoxomolybdate Clusters. Shown in Figure 5 are the experimental and predicted CCS values for singly charged polyoxomolybdate clusters, $\text{HMo}_n\text{O}_{3n+1}^{1-}$ ($n = 1-8$) plotted with respect to cluster size n . For comparison, the CCS values for the doubly charged $\text{Mo}_n\text{O}_{3n+1}^{2-}$ ($n = 2-8$) are shown as well. Compared to the doubly charged clusters, the evolution of CCS with cluster size is much smoother for the singly charged clusters. In particular, sharp discontinuities in CCS values are not observed between $n = 3$ and $n = 4$ or between $n = 5$ and $n = 6$. When comparing the CCS of singly charged clusters to the ones of the corresponding doubly charged species, the largest differences are observed for $n = 3$ and $n = 5$, for which the CCS values of the singly charged clusters are 17 and 20% lower, respectively. For the doubly charged clusters $\text{Mo}_n\text{O}_{3n+1}^{2-}$, structural transitions to cyclic and three-dimensional compact clusters occur for $n = 4$ and $n = 6$, respectively. The large differences in CCS values between singly and doubly charged clusters for $n = 3$ and $n = 5$ could be explained by an earlier transition to cyclic and compact clusters, already occurring at those sizes.

Shown as circles in Figure 5 are CCS values calculated for low-energy theoretical structures (see Figure 6). Examining the structures yields interesting differences, compared to the

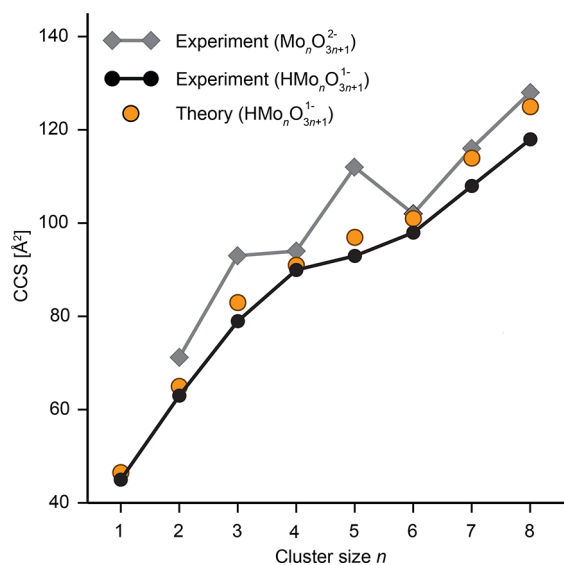


Figure 5. Comparison of experimental and theoretical CCS values for singly charged polyoxomolybdate clusters $\text{HMo}_n\text{O}_{3n+1}^{1-}$ ($n = 1-8$) as well as experimental CCS values for doubly charged polyoxomolybdate clusters $\text{Mo}_n\text{O}_{3n+1}^{2-}$ ($n = 2-8$). CCS values are plotted as a function of the number of molybdenum atoms in the cluster n , with experimental values for $\text{Mo}_n\text{O}_{3n+1}^{2-}$ and $\text{HMo}_n\text{O}_{3n+1}^{1-}$ plotted as black diamonds and circles, respectively. Predicted CCS values for model structures of $\text{HMo}_n\text{O}_{3n+1}^{1-}$ clusters are plotted as orange circles.

doubly charged clusters. Theory predicts $\text{HMo}_3\text{O}_{10}^{1-}$ to indeed form a ring-like structure. However, the ring is formed by a bridging proton, which is bound to one oxygen with a bond length of 1.08 Å and is strongly hydrogen bound to an oxygen atom at the other end of the cluster with a hydrogen bond length of 1.39 Å. For $\text{HMo}_5\text{O}_{16}^{1-}$, theory predicts a compact structure, in which the fifth molybdenum oxide unit is situated directly above a ring of four molybdenum oxide units. In the doubly charged $\text{Mo}_5\text{O}_{16}^{2-}$ cluster, this fifth unit is predicted to reside either outside a ring of four molybdenum oxide units (Figure S2b) or as a constituent of the ring (Figure S2c,d), suggesting that the increased Coulombic repulsion in the doubly charged cluster destabilizes a compact conformation.

The structure of the singly charged polyoxomolybdate clusters were also investigated using infrared action spectroscopy (Figure 6). Spectra were acquired for cluster sizes $n = 1-8$ using the IRMPD method (red spectra), as CCS/ z selection prior to IR irradiation provided separation of singly and doubly charged species with overlapping m/z . However, spectra collected by IR action spectroscopy in He nanodroplets were obtained only for $n = 1-3$ (blue spectra), as singly and doubly charged clusters with overlapping isotopic envelopes could not be probed individually in the experimental setup. The spectra predicted in the harmonic approximation for low-energy DFT structures are shown in gray for each cluster size, with the corresponding structure displayed to the right of the spectrum. Similar to the doubly charged clusters, a blue-shift of the terminal oxygen stretching modes is observed with increasing cluster size, and good agreement is observed between the predicted and experimental values for these modes.

For the smaller singly charged clusters for which He nanodroplet spectra were recorded, the cold-ion and theoretical spectra likewise show good agreement. For HMoO_4^{1-} , the cold IR spectrum shows only one band, while theory predicts a doublet accompanied by a weak satellite

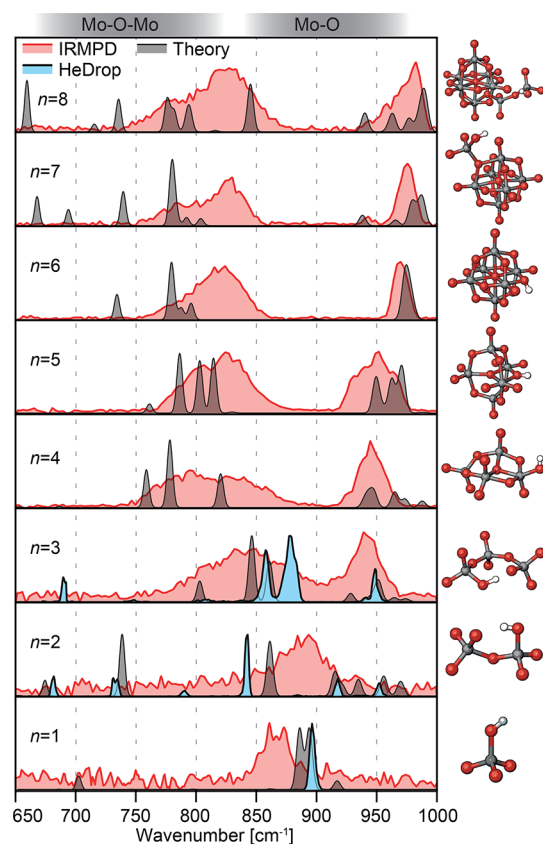


Figure 6. Action infrared spectra of $\text{HMo}_n\text{O}_{3n+1}^-$ obtained utilizing IRMPD spectroscopy of room-temperature ions (red, $n = 1-8$) and IR spectroscopy of ions captured in helium nanodroplets (blue, $n = 1-3$) compared with unscaled theoretical IR spectra convoluted with Gaussian distributions with full width at half-maximum values of 0.7% (gray). The corresponding structure for each theoretical spectrum is shown at right.

band. A possible explanation for this discrepancy lies in the dynamic nature of the HMoO_4^{1-} ion. The O–H acts as an internal rotor. Theory predicts that the barrier for rotation is very low ($\sim 50 \text{ cm}^{-1}$ at the MP2^{74,75} level and $\sim 30 \text{ cm}^{-1}$ at the B3LYP^{76,77} level, using the def2-TZVP basis set;^{78,79} as a comparison, the barrier height for OH rotation in methanol is $\sim 370 \text{ cm}^{-1}$). This might be below the zero-point level of that mode, resulting in free rotation, an effective increase in symmetry, and decrease of the number of distinct modes. Interestingly, for $\text{HMo}_2\text{O}_7^{1-}$, four bands are predicted for the Mo–O stretching modes due to the structural asymmetry induced by the localized proton. However, only two bands are observed in the Mo–O stretching region in the He nanodroplet spectrum, suggesting a more symmetric structure, in which the proton is shared between oxygen moieties. For $\text{HMo}_3\text{O}_{10}^{1-}$, the experimental and theoretical spectra show good agreement, further supporting the predicted noncovalent conformation featuring a strong intramolecular hydrogen bond. For larger clusters, for which only IRMPD spectra were acquired, a qualitative agreement between experiment and theory is also observed. In contrast to the doubly charged clusters, modified Lindqvist structures for $\text{HMo}_7\text{O}_{22}^{1-}$ and $\text{HMo}_8\text{O}_{25}^{1-}$ were found to be more stable than other candidate structures. Although the lack of cold-ion spectra hinders a detailed structural assignment, the combination of IRMPD and

IMS–MS data yields a high degree of confidence in the overall geometry observed at each cluster size.

An important question is in how far do the here observed gas-phase structures have a relationship to those observed in the condensed phase. When comparing the gas-phase singly and doubly charged clusters, structural differences are observed that stem from Coulombic repulsion and the ability to form intramolecular hydrogen bonds. These interactions become even more crucial in the condensed phase, where it is observed that the choice of solvent and counterions can influence the structure in a defined way.⁸⁰ Nonetheless, there are quite some structural similarities between the here observed solvent as well as counterion free structures and the structures observed in the solid state.

For the Mo_2 and Mo_3 species, chain-like structures are observed in the gas phase. Similarly, the well-known crystal structures of di and trimolybdates in the solid state are composed of infinite polyhedral chains, however, showing considerable structural variety in connecting MoO_4 , MoO_5 , and MoO_6 units.^{81,82} Hydrothermal synthesis has been applied to tune the arrangement of the polyhedra by varying the nature of the counterion.⁸³ The basic units of the molybdenum–oxygen framework in crystalline di and trimolybdates correspond to the di and trinuclear species detected in the gas phase, whereas here, the molecular polyhedral arrangement adopts an equilibrium structure, because the Mo–O framework is not imposed by constraints due to the presence of counterions.

In the case of Mo_4 , the structure of the tetranuclear building block $\text{Mo}_4\text{O}_{13}^{2-}$ in the gas phase resembles the tetrameric unit in crystalline diammonium tetramolybdate prepared by hydrothermal synthesis.⁸⁴ The solid is formed by self-assembly of chains composed of $\text{Mo}_4\text{O}_{13}^{2-}$ units. Again, the intrinsic molecular structure of the unit with respect to polyhedral connection depends on synthesis and counterion and reveals a considerable structural diversity of crystal structures based on $\text{Mo}_4\text{O}_{13}^{2-}$.⁸⁵

The here presented results on the Mo_5 species show that those species have a large structural variety, being cyclic for $\text{Mo}_5\text{O}_{16}^{2-}$ and compact for $\text{HMo}_5\text{O}_{16}^{1-}$ and with many low-energy isomers predicted by theory. This transient nature of the pentamolybdate species is in agreement with a considerable structural variety of pentamolybdates in the solid state.^{86–89}

Finally for the hexamolybdate and larger species, structures based on the Lindqvist motif are observed in the gas phase. In the condensed phase, such a structure can be isolated by synthesis in nonaqueous environment or in the presence of large counterions.⁹⁰

CONCLUSIONS

In summary, we report here an investigation of the structures of small polyoxomolybdate ions in the gas phase using the combination of ESI-IMS–MS, IRMPD, IR action spectroscopy in helium nanodroplets, and ab initio methods. Transfer of the species from solution to the gas phase allows for the structural interrogation of isolated cluster ions, circumventing the complexity and polydispersity encountered in traditional condensed-phase methods. Specifically, the ESI-IMS–MS method reveals transitions in the coordination of molybdenum oxide units with increasing cluster size. The infrared spectra collected in helium nanodroplets yield well-resolved spectral lines even for large cluster ions, providing potential benchmarks for theoretical calculations and spectroscopic character-

ization of functional materials. Moreover, these highly resolved spectra show the potential of the helium nanodroplet method for characterization of the structure of catalytic nanoclusters or transient short-lived species. For doubly charged clusters, all experimental methods as well as theoretical predictions support transitions among chain, ring, and compact structural motifs as the number of molybdenum oxide units in the cluster increases. The addition of a single proton to form singly charged anion clusters is observed to strongly influence the adopted structure for some cluster sizes as a result of intramolecular hydrogen bonding and reduced Coulombic repulsion. When comparing the here observed structures to those in the condensed phase, we observe that some of the gas-phase structures correspond to building units constituting the molybdenum oxide framework of well-known crystalline molybdate phases; however, structural rearrangements in the absence of solvation and crystal field effects are observed. The approach presented shows the utility of combining IMS–MS and IR action spectroscopy to obtain structural insights into metal oxide nanoclusters.

■ ASSOCIATED CONTENT

Supporting Information

The Supporting Information is available free of charge on the ACS Publications website at DOI: 10.1021/acs.jpcc.8b06985.

Cartesian coordinates and vibrational frequencies from DFT optimization in the FHI-aims program (TXT) Additional details of ab initio methods, ion arrival time distributions and CCSs, theoretical IR spectra of additional conformations of $\text{Mo}_5\text{O}_{16}^{2-}$, $\text{Mo}_7\text{O}_{22}^{2-}$, and $\text{Mo}_8\text{O}_{25}^{2-}$, CCS vs energy plot for $\text{Mo}_8\text{O}_{25}^{2-}$ structures (PDF)

■ AUTHOR INFORMATION

Corresponding Authors

*E-mail: trunschke@fhi-berlin.mpg.de (A.T.)

*E-mail: helden@fhi-berlin.mpg.de (G.v.H.)

ORCID

Jongcheol Seo: 0000-0001-5844-4585

Daniel A. Thomas: 0000-0001-9415-5991

Gerard Meijer: 0000-0001-9669-8340

Annette Trunschke: 0000-0003-2869-0181

Gert von Helden: 0000-0001-7611-8740

Author Contributions

[†]M.M. and J.S. contributed equally to this work

Notes

The authors declare no competing financial interest.

■ ACKNOWLEDGMENTS

The authors thank Sandy Gewinner and Wieland Schöllkopf of the FHI FEL for laser operation. This work was conducted in the framework of the BasCat collaboration between BASF SE, TU Berlin, FHI and the cluster of excellence “Unifying Concepts in Catalysis” (UniCat www.unicat.tu-berlin.de). D.A.T. gratefully acknowledges support from the Alexander von Humboldt Foundation. M.M. is grateful to Matthias Scheffler (FHI) for support of the computational work.

■ REFERENCES

(1) Coronado, E.; Gómez-García, C. J. Polyoxometalate-Based Molecular Materials. *Chem. Rev.* **1998**, *98*, 273–296.

(2) Kozhevnikov, I. V. Catalysis by Heteropoly Acids and Multicomponent Polyoxometalates in Liquid-Phase Reactions. *Chem. Rev.* **1998**, *98*, 171–198.

(3) Mizuno, N.; Misono, M. Heterogeneous Catalysis. *Chem. Rev.* **1998**, *98*, 199–218.

(4) Sadakane, M.; Steckhan, E. Electrochemical Properties of Polyoxometalates as Electrocatalysts. *Chem. Rev.* **1998**, *98*, 219–238.

(5) Katsoulis, D. E. A Survey of Applications of Polyoxometalates. *Chem. Rev.* **1998**, *98*, 359–388.

(6) Rhule, J. T.; Hill, C. L.; Judd, D. A.; Schinazi, R. F. Polyoxometalates in Medicine. *Chem. Rev.* **1998**, *98*, 327–358.

(7) Keggin, J. F. Structure of the Molecule of 12-Phosphotungstic Acid. *Nature* **1933**, *131*, 908–909.

(8) Hasenknopf, B.; Delmont, R.; Herson, P.; Gouzerh, P. Anderson-Type Heteropolymolybdates Containing Tris(alkoxo) Ligands: Synthesis and Structural Characterization. *Eur. J. Inorg. Chem.* **2002**, *2002*, 1081–1087.

(9) Marcoux, P. R.; Hasenknopf, B.; Vaissermann, J.; Gouzerh, P. Developing Remote Metal Binding Sites in Heteropolymolybdates. *Eur. J. Inorg. Chem.* **2003**, *2003*, 2406–2412.

(10) Hou, Y.; Hill, C. L. Hydrolytically Stable Organic Triester Capped Polyoxometalates with Catalytic Oxygenation Activity of Formula $[\text{RC}(\text{CH}_2\text{O})_3\text{V}_3\text{P}_2\text{W}_{15}\text{O}_{59}]^{6-}$ (R = CH₃, NO₂, CH₂OH). *J. Am. Chem. Soc.* **1993**, *115*, 11823–11830.

(11) Zeng, H.; Newkome, G. R.; Hill, C. L. Poly(polyoxometalate) Dendrimers: Molecular Prototypes of New Catalytic Materials. *Angew. Chem., Int. Ed.* **2000**, *39*, 1771–1774.

(12) Chen, Q.; Goshorn, D. P.; Scholes, C. P.; Tan, X. L.; Zubieta, J. Coordination Compounds of Polyoxovanadates with a Hexametalate Core. Chemical and Structural Characterization of $[\text{V}_6\text{O}_{13}[(\text{OCH}_2)_3\text{CR}]_2]^{2-}$, $[\text{V}_6\text{O}_{11}(\text{OH})_2[(\text{OCH}_2)_3\text{CR}]_2]$, $[\text{V}^{\text{IV}}_4\text{V}^{\text{V}}_2\text{O}_9(\text{OH})_4[(\text{OCH}_2)_3\text{CR}]_2]^{2-}$, and $[\text{V}^{\text{IV}}_6\text{O}_7(\text{OH})_6[(\text{OCH}_2)_3\text{CR}]_2]^{2-}$. *J. Am. Chem. Soc.* **1992**, *114*, 4667–4681.

(13) Khan, M. I.; Chen, Q.; Zubieta, J.; Goshorn, D. P. Hexavanadium Polyoxoalkoxide Anion Clusters: Structures of the Mixed-Valence Species $(\text{Me}_3\text{NH})[\text{V}^{\text{IV}}_5\text{V}^{\text{V}}\text{O}_7(\text{OH})_3\text{CH}_3\text{C}(\text{CH}_2\text{O})_{33}]$ and of the Reduced Complex $\text{Na}_2[\text{V}^{\text{IV}}_6\text{O}_7\{\text{CH}_3\text{CH}_2\text{C}(\text{CH}_2\text{O})_3\}_4]$. *Inorg. Chem.* **1992**, *31*, 1556–1558.

(14) Bleiholder, C.; Dupuis, N. F.; Wyttenbach, T.; Bowers, M. T. Ion Mobility-Mass Spectrometry Reveals a Conformational Conversion from Random Assembly to β -Sheet in Amyloid Fibril Formation. *Nat. Chem.* **2011**, *3*, 172–177.

(15) Wu, J. W. J.; Moriyama, R.; Nakano, M.; Ohshimo, K.; Misaizu, F. Compositions and Structures of Niobium Oxide Cluster Ions, $\text{Nb}_m\text{O}_n^\pm$ (m = 2–12), Revealed by Ion Mobility Mass Spectrometry. *Phys. Chem. Chem. Phys.* **2017**, *19*, 24903–24914.

(16) Oomens, J.; Sartakov, B. G.; Meijer, G.; von Helden, G. Gas-Phase Infrared Multiple Photon Dissociation Spectroscopy of Mass-Selected Molecular Ions. *Int. J. Mass Spectrom.* **2006**, *254*, 1–19.

(17) Seo, J.; Jang, J.; Warnke, S.; Gewinner, S.; Schöllkopf, W.; von Helden, G. Stacking Geometries of Early Protoporphyrin IX Aggregates Revealed by Gas-Phase Infrared Spectroscopy. *J. Am. Chem. Soc.* **2016**, *138*, 16315–16321.

(18) Seo, J.; Hoffmann, W.; Warnke, S.; Huang, X.; Gewinner, S.; Schöllkopf, W.; Bowers, M. T.; von Helden, G.; Pagel, K. An Infrared Spectroscopy Approach to Follow β -Sheet Formation in Peptide Amyloid Assemblies. *Nat. Chem.* **2016**, *9*, 39–44.

(19) González Flórez, A. I.; Ahn, D.-S.; Gewinner, S.; Schöllkopf, W.; von Helden, G. IR Spectroscopy of Protonated Leu-enkephalin and its 18-crown-6 Complex Embedded in Helium Droplets. *Phys. Chem. Chem. Phys.* **2015**, *17*, 21902–21911.

(20) Mucha, E.; González Flórez, A. I.; Marianski, M.; Thomas, D. A.; Hoffmann, W.; Struwe, W. B.; Hahm, H. S.; Gewinner, S.; Schöllkopf, W.; Seeberger, P. H. Glycan Fingerprinting via Cold-Ion Infrared Spectroscopy. *Angew. Chem., Int. Ed.* **2017**, *56*, 11248–11251.

(21) Thomas, D. A.; Mucha, E.; Gewinner, S.; Schöllkopf, W.; Meijer, G.; von Helden, G. Vibrational Spectroscopy of Fluorofor-

mate, FCO_2^- , Trapped in Helium Nanodroplets. *J. Phys. Chem. Lett.* **2018**, *9*, 2305–2310.

(22) Thomas, D. A.; Marianski, M.; Mucha, E.; Meijer, G.; Johnson, M. A.; von Helden, G. Ground-State Structure of the Proton-Bound Formate Dimer by Cold-Ion Infrared Action Spectroscopy. *Angew. Chem., Int. Ed.* **2018**, *57*, 10615–10619.

(23) Hernandez, O.; Isenberg, S.; Steinmetz, V.; Glish, G. L.; Maitre, P. Probing Mobility-Selected Saccharide Isomers: Selective Ion–Molecule Reactions and Wavelength-Specific IR Activation. *J. Phys. Chem. A* **2015**, *119*, 6057–6064.

(24) Schubert, F.; Rossi, M.; Baldauf, C.; Pagel, K.; Warnke, S.; von Helden, G.; Filsinger, F.; Kupser, P.; Meijer, G.; Salwiczek, M.; et al. Exploring the Conformational Preferences of 20-Residue Peptides in Isolation: Ac-Ala₁₉-Lys + H⁺ vs. Ac-Lys-Ala₁₉ + H⁺ and the Current Reach of DFT. *Phys. Chem. Chem. Phys.* **2015**, *17*, 7373–7385.

(25) Hoffmann, W.; Marianski, M.; Warnke, S.; Seo, J.; Baldauf, C.; von Helden, G.; Pagel, K. Assessing the Stability of Alanine-based Helices by Conformer-Selective IR Spectroscopy. *Phys. Chem. Chem. Phys.* **2016**, *18*, 19950–19954.

(26) Walanda, D. K.; Burns, R. C.; Lawrance, G. A.; von Nagy-Felsobuki, E. I. New Isopolyoxovanadate Ions Identified by Electrospray Mass Spectrometry. *Inorg. Chem. Commun.* **1999**, *2*, 487–489.

(27) Walanda, D. K.; Burns, R. C.; Lawrance, G. A.; von Nagy-Felsobuki, E. I. Electrospray Mass Spectral Study of Isopolyoxomolybdates. *J. Chem. Soc., Dalton Trans.* **1999**, 311–322.

(28) Bussian, P.; Sobott, F.; Brutschy, B.; Schrader, W.; Schüth, F. Speciation in Solution: Silicate Oligomers in Aqueous Solutions Detected by Mass Spectrometry. *Angew. Chem., Int. Ed.* **2000**, *39*, 3901–3905.

(29) Pelster, S. A.; Schrader, W.; Schüth, F. Monitoring Temporal Evolution of Silicate Species during Hydrolysis and Condensation of Silicates Using Mass Spectrometry. *J. Am. Chem. Soc.* **2006**, *128*, 4310–4317.

(30) Rood, J. A.; Bogges, W. C.; Noll, B. C.; Henderson, K. W. Assembly of a Homochiral, Body-Centered Cubic Network Composed of Vertex-Shared Mg₁₂ Cages: Use of Electrospray Ionization Mass Spectrometry to Monitor Metal Carboxylate Nucleation. *J. Am. Chem. Soc.* **2007**, *129*, 13675–13682.

(31) Miras, H. N.; Wilson, E. F.; Cronin, L. Unravelling the Complexities of Inorganic and Supramolecular Self-Assembly in Solution with Electrospray and Cryospray Mass Spectrometry. *Chem. Commun.* **2009**, 1297–1311.

(32) Vilá-Nadal, L.; Rodríguez-Fortea, A.; Yan, L.-K.; Wilson, E. F.; Cronin, L.; Poblet, J. Nucleation Mechanisms of Molecular Oxides: A Study of the Assembly-Dissassembly of $[\text{W}_6\text{O}_{19}]^{2-}$ by Theory and Mass Spectrometry. *Angew. Chem., Int. Ed.* **2009**, *48*, 5452–5456.

(33) Vilá-Nadal, L.; Wilson, E. F.; Miras, H. N.; Rodríguez-Fortea, A.; Cronin, L.; Poblet, J. M. Combined Theoretical and Mass Spectrometry Study of the Formation-Fragmentation of Small Polyoxomolybdates. *Inorg. Chem.* **2011**, *50*, 7811–7819.

(34) Wilson, E. F.; Miras, H. N.; Rosnes, M. H.; Cronin, L. Real-Time Observation of the Self-Assembly of Hybrid Polyoxometalates Using Mass Spectrometry. *Angew. Chem., Int. Ed.* **2011**, *50*, 3720–3724.

(35) Miras, H. N.; Sorus, M.; Hawkett, J.; Sells, D. O.; McInnes, E. J. L.; Cronin, L. Oscillatory Template Exchange in Polyoxometalate Capsules: A Ligand-Triggered, Redox-Powered, Chemically Damped Oscillation. *J. Am. Chem. Soc.* **2012**, *134*, 6980–6983.

(36) Gao, J.; Yan, J.; Beeg, S.; Long, D.-L.; Cronin, L. Assembly of Molecular “Layered” Heteropolyoxometalate Architectures. *Angew. Chem., Int. Ed.* **2012**, *51*, 3373–3376.

(37) Corella-Ochoa, M. N.; Miras, H. N.; Long, D.-L.; Cronin, L. Controlling the Self-Assembly of a Mixed-Metal Mo/V-Selenite Family of Polyoxometalates. *Chem. - Eur. J.* **2012**, *18*, 13743–13754.

(38) Winter, R. S.; Cameron, J. M.; Cronin, L. Controlling the Minimal Self Assembly of “Complex” Polyoxometalate Clusters. *J. Am. Chem. Soc.* **2014**, *136*, 12753–12761.

(39) Nakamura, I.; Miras, H. N.; Fujiwara, A.; Fujibayashi, M.; Song, Y.-F.; Cronin, L.; Tsunashima, R. Investigating the Formation of “Molybdenum Blues” with Gel Electrophoresis and Mass Spectrometry. *J. Am. Chem. Soc.* **2015**, *137*, 6524–6530.

(40) Cameron, J. M.; Vilá-Nadal, L.; Winter, R. S.; Iijima, F.; Murillo, J. C.; Rodríguez-Fortea, A.; Oshio, H.; Poblet, J. M.; Cronin, L. Investigating the Transformations of Polyoxoanions Using Mass Spectrometry and Molecular Dynamics. *J. Am. Chem. Soc.* **2016**, *138*, 8765–8773.

(41) Wendt, M.; Warzok, U.; Näther, C.; van Leusen, J.; Kögerler, P.; Schalley, C. A.; Bensch, W. Catalysis of “Outer-Phase” Oxygen Atom Exchange Reactions by Encapsulated “Inner-Phase” Water in $\{\text{V}_1\text{Sb}_6\}$ -Type Polyoxovanadates. *Chem. Sci.* **2016**, *7*, 2684–2694.

(42) Schaack, B. B.; Schrader, W.; Corma, A.; Schüth, F. Nucleation of ITQ-21 Studied by ESI-MS. *Chem. Mater.* **2009**, *21*, 4448–4453.

(43) Lim, I. H.; Schrader, W.; Schüth, F. The Formation of Zeolites from Solution - Analysis by Mass Spectrometry. *Microporous Mesoporous Mater.* **2013**, *166*, 20–36.

(44) Lim, I. H.; Schrader, W.; Schüth, F. Insights into the Molecular Assembly of Zeolitic Imidazolate Frameworks by ESI-MS. *Chem. Mater.* **2015**, *27*, 3088–3095.

(45) Thiel, J.; Yang, D.; Rosnes, M. H.; Liu, X.; Yvon, C.; Kelly, S. E.; Song, Y.-F.; Long, D.-L.; Cronin, L. Observing the Hierarchical Self-Assembly and Architectural Bistability of Hybrid Molecular Metal Oxides Using Ion-Mobility Mass Spectrometry. *Angew. Chem., Int. Ed.* **2011**, *50*, 8871–8875.

(46) McGlone, T.; Thiel, J.; Streb, C.; Long, D.-L.; Cronin, L. An Unprecedented Silver-Decavanadate Dimer Investigated Using Ion-Mobility Mass Spectrometry. *Chem. Commun.* **2012**, 48, 359–361.

(47) Robbins, P. J.; Surman, A. J.; Thiel, J.; Long, D.-L.; Cronin, L. Use of Ion-Mobility Mass Spectrometry (IMS-MS) to Map Polyoxometalate Keplerate Clusters and Their Supramolecular Assemblies. *Chem. Commun.* **2013**, 49, 1909–1911.

(48) Surman, A. J.; Robbins, P. J.; Ujma, J.; Zheng, Q.; Barran, P. E.; Cronin, L. Sizing and Discovery of Nanosized Polyoxometalate Clusters by Mass Spectrometry. *J. Am. Chem. Soc.* **2016**, *138*, 3824–3830.

(49) Fielicke, A.; Kirilyuk, A.; Ratsch, C.; Behler, J.; Scheffler, M.; von Helden, G.; Meijer, G. Structure Determination of Isolated Metal Clusters via Far-Infrared Spectroscopy. *Phys. Rev. Lett.* **2004**, *93*, 023401.

(50) Fielicke, A.; von Helden, G.; Meijer, G.; Pedersen, D. B.; Simard, B.; Rayner, D. M. Gold Cluster Carbonyls: Saturated Adsorption of CO on Gold Cluster Cations, Vibrational Spectroscopy, and Implications for Their Structures. *J. Am. Chem. Soc.* **2005**, *127*, 8416–8423.

(51) Kirilyuk, A.; Fielicke, A.; Demyk, K.; von Helden, G.; Meijer, G.; Rasing, T. Ferrimagnetic Cage-like Fe₄O₆ Cluster: Structure Determination from Infrared Dissociation Spectroscopy. *Phys. Rev. B: Condens. Matter Mater. Phys.* **2010**, *82*, 020405.

(52) Asmis, K. R.; Santambrogio, G.; Brümmer, M.; Sauer, J. Polyhedral Vanadium Oxide Cages: Infrared Spectra of Cluster Anions and Size-Induced d Electron Localization. *Angew. Chem., Int. Ed.* **2005**, *44*, 3122–3125.

(53) Fielicke, A.; Meijer, G.; von Helden, G. Infrared Multiple Photon Dissociation Spectroscopy of Transition Metal Oxide Cluster Cations. *Eur. Phys. J. D* **2003**, *24*, 69–72.

(54) Wen, X.-D.; Martin, R. L.; Henderson, T. M.; Scuseria, G. E. Density Functional Theory Studies of the Electronic Structure of Solid State Actinide Oxides. *Chem. Rev.* **2013**, *113*, 1063–1096.

(55) Jain, A.; Shin, Y.; Persson, K. A. Computational Predictions of Energy Materials Using Density Functional Theory. *Nat. Rev. Mater.* **2016**, *1*, 15004.

(56) Broclawik, E. On the Electronic Structure of Transition-Metal Oxide Cations: DFT Calculations for VO⁺ and MoO⁺. *Int. J. Quantum Chem.* **1995**, *56*, 779–785.

(57) Bhattacharya, S.; Levchenko, S. V.; Ghiringhelli, L. M.; Scheffler, M. Stability and Metastability of Clusters in a Reactive

Atmosphere: Theoretical Evidence for Unexpected Stoichiometries of Mg_mO_x . *Phys. Rev. Lett.* **2013**, *111*, 135501.

(58) Fagiani, M. R.; Song, X.; Debnath, S.; Gewinner, S.; Schöllkopf, W.; Asmis, K. R.; Bischoff, F. A.; Müller, F.; Sauer, J. Dissociative Water Adsorption by Al_3O_4^+ in the Gas Phase. *J. Phys. Chem. Lett.* **2017**, *8*, 1272–1277.

(59) Warnke, S.; Seo, J.; Boschmans, J.; Sobott, F.; Scrivens, J. H.; Bleiholder, C.; Bowers, M. T.; Gewinner, S.; Schöllkopf, W.; Pagel, K.; et al. Protomers of Benzocaine: Solvent and Permittivity Dependence. *J. Am. Chem. Soc.* **2015**, *137*, 4236–4242.

(60) Warnke, S.; von Helden, G.; Pagel, K. Analyzing the Higher Order Structure of Proteins with Conformer-Selective Ultraviolet Photodissociation. *Proteomics* **2015**, *15*, 2804–2812.

(61) Schöllkopf, W.; Gewinner, S.; Junkes, H.; Paarmann, A.; von Helden, G.; Blum, H.; Todd, A. M. M. The New IR and THz FEL Facility at the Fritz Haber Institute in Berlin. *Proc. SPIE* **2015**, *9512*, 95121L.

(62) González Flórez, A. I.; Mucha, E.; Ahn, D.; Gewinner, S.; Schöllkopf, W.; Pagel, K.; von Helden, G. Charge-Induced Unzipping of Isolated Proteins to a Defined Secondary Structure. *Angew. Chem., Int. Ed.* **2016**, *55*, 3295–3299.

(63) González Flórez, A. I. Biomolecular Ions in Superfluid Helium Nanodroplets. Ph.D. Thesis, Freie Universität, Berlin, 2016.

(64) Perdew, J. P.; Burke, K.; Ernzerhof, M. Generalized Gradient Approximation Made Simple. *Phys. Rev. Lett.* **1996**, *77*, 3865–3868.

(65) Tkatchenko, A.; Scheffler, M. Accurate Molecular Van Der Waals Interactions from Ground-State Electron Density and Free-Atom Reference Data. *Phys. Rev. Lett.* **2009**, *102*, 73005.

(66) Blum, V.; Gehrke, R.; Hanke, F.; Havu, P.; Havu, V.; Ren, X.; Reuter, K.; Scheffler, M. Ab Initio Molecular Simulations with Numeric Atom-Centered Orbitals. *Comput. Phys. Commun.* **2009**, *180*, 2175–2196.

(67) von Helden, G.; Hsu, M. T.; Gotts, N.; Bowers, M. T. Carbon Cluster Cations with Up to 84 atoms: Structures, Formation Mechanism, and Reactivity. *J. Phys. Chem.* **1993**, *97*, 8182–8192.

(68) Christodoulakis, A.; Heracleous, E.; Lemonidou, A. A.; Boghosian, S. An Operando Raman Study of Structure and Reactivity of Alumina-Supported Molybdenum Oxide Catalysts for the Oxidative Dehydrogenation of Ethane. *J. Catal.* **2006**, *242*, 16–25.

(69) Vuurman, M. A.; Wachs, I. E. In Situ Raman Spectroscopy of Alumina Support Metal Oxide Catalysts. *J. Phys. Chem.* **1992**, *96*, 5008–5016.

(70) Handzlik, J.; Sautet, P. Structure of Dimeric Molybdenum(VI) Oxide Species on gamma-Alumina: A Periodic Density Functional Theory Study. *J. Phys. Chem. C* **2010**, *114*, 19406–19414.

(71) Freund, H.-J. The Surface Science of Catalysis and More, Using Ultrathin Oxide Films as Templates: A Perspective. *J. Am. Chem. Soc.* **2016**, *138*, 8985–8996.

(72) Guo, C. S.; Hermann, K.; Hävecker, M.; Thielemann, J. P.; Kube, P.; Gregoriades, L. J.; Trunschke, A.; Sauer, J.; Schlögl, R. Structural Analysis of Silica-Supported Molybdena Based on X-ray Spectroscopy: Quantum Theory and Experiment. *J. Phys. Chem. C* **2011**, *115*, 15449–15458.

(73) Amakawa, K.; Sun, L.; Guo, C.; Hävecker, M.; Kube, P.; Wachs, I. E.; Lwin, S.; Frenkel, A. I.; Patlolla, A.; Hermann, K.; et al. How Strain Affects the Reactivity of Surface Metal Oxide Catalysts. *Angew. Chem., Int. Ed.* **2013**, *52*, 13553–13557.

(74) Møller, C.; Plesset, M. S. Note on an Approximation Treatment for Many-Electron Systems. *Phys. Rev.* **1934**, *46*, 618–622.

(75) Bartlett, R. J. Many-Body Perturbation Theory and Coupled Cluster Theory for Electron Correlation in Molecules. *Annu. Rev. Phys. Chem.* **1981**, *32*, 359–401.

(76) Becke, A. D. Density-Functional Thermochemistry. III. The Role of Exact Exchange. *J. Chem. Phys.* **1993**, *98*, 5648–5652.

(77) Stephens, P. J.; Devlin, F. J.; Chabalowski, C. F.; Frisch, M. J. Ab Initio Calculation of Vibrational Absorption and Circular Dichroism Spectra Using Density Functional Force Fields. *J. Phys. Chem.* **1994**, *98*, 11623–11627.

(78) Weigend, F.; Ahlrichs, R. Balanced Basis Sets of Split Valence, Triple Zeta Valence and Quadruple Zeta Valence Quality for H to Rn: Design and Assessment of Accuracy. *Phys. Chem. Chem. Phys.* **2005**, *7*, 3297–3305.

(79) Weigend, F. Accurate Coulomb-Fitting Basis Sets for H to Rn. *Phys. Chem. Chem. Phys.* **2006**, *8*, 1057–1065.

(80) Cruywagen, J. J. Protonation, Oligomerization, and Condensation Reactions of Vanadate(V), Molybdate(VI), and Tungstate(VI). *Adv. Inorg. Chem.* **1999**, *49*, 127–182.

(81) Day, V. W.; Fredrich, M. F.; Klemperer, W. G.; Shum, W. Synthesis and Characterization of the Dimolybdate Ion, $\text{Mo}_2\text{O}_7^{2-}$. *J. Am. Chem. Soc.* **1977**, *99*, 6146–6148.

(82) Wang, M.; You, J.; Sobol, A. A.; Wang, J.; Wu, J.; Lv, X. Temperature-Dependent Raman Spectroscopic Studies of Microstructure Present in Dipotassium Molybdate Crystals and Their Melts. *J. Raman Spectrosc.* **2016**, *47*, 1259–1265.

(83) Michailovski, A.; Patzke, G. R. Hydrothermal Synthesis and Crystal Structure of Novel Alkali Trimolybdates. *Z. Anorg. Allg. Chem.* **2007**, *633*, 54–62.

(84) Briceño, A.; Atencio, R. $[(\text{NH}_4)_2(\text{Mo}_4\text{O}_{13})]_n$: A Novel Two-Dimensional Polyoxomolybdate(VI) Framework. *Acta Crystallogr., Sect. E: Struct. Rep. Online* **2004**, *60*, 147–149.

(85) Zapf, P. J.; LaDuca, R. L.; Rarig, R. S.; Johnson, K. M.; Zubieta, J. A Two-Dimensional Network Constructed via Hydrogen-Bonded Cross-Linkages of Molybdenum Oxide Chains. *Inorg. Chem.* **1998**, *37*, 3411–3414.

(86) Gatehouse, B. M.; Miskin, B. K. Crystal Structures of Cesium Pentamolybdate, $\text{Cs}_2\text{Mo}_5\text{O}_{16}$, and Cesium Heptamolybdate, $\text{Cs}_2\text{Mo}_7\text{O}_{22}$. *Acta Crystallogr., Sect. B: Struct. Crystallogr. Cryst. Chem.* **1975**, *31*, 1293–1299.

(87) Dessapt, R.; Kervern, D.; Bujoli-Doeuff, M.; Deniard, P.; Evain, M.; Jobic, S. How Does the Synthesis Temperature Impact Hybrid Organic-Inorganic Molybdate Material Design? *Inorg. Chem.* **2010**, *49*, 11309–11316.

(88) Yang, M.-X.; Lin, S.; Chen, L.-J.; Zhang, X.-F.; Huang, H. Two Novel 3D Bimetallic Oxide Framework with 16-Membered Wheel Clusters Based on Mo_5O_{16} Ribbon-Like Chains. *Inorg. Chem. Commun.* **2011**, *14*, 1652–1655.

(89) Oszajca, M.; Smrčok, L.; Łasocha, W. Bis(4-methylanilinium) and Bis(4-iodoanilinium) Pentamolybdates from Laboratory X-ray Powder Data and Total Energy Minimization. *Acta Crystallogr., Sect. C: Cryst. Struct. Commun.* **2013**, *69*, 1367–1372.

(90) Clegg, W.; Sheldrick, G. M.; Garner, C. D.; Walton, I. B. Structure of Bis(tetraphenylarsonium) Hexamolybdate(VI). *Acta Crystallogr., Sect. B: Struct. Crystallogr. Cryst. Chem.* **1982**, *38*, 2906–2909.